Methylamine-Gas-Induced Defect-Healing Behavior of $CH_3NH_3PbI_3$ Thin Films for Perovskite Solar Cells**

Zhongmin Zhou, Zaiwei Wang, Yuanyuan Zhou, Shuping Pang,* Dong Wang, Hongxia Xu, Zhihong Liu, Nitin P. Padture, and Guanglei Cui*

Abstract: We report herein the discovery of methylamine (CH_3NH_2) induced defect-healing (MIDH) of $CH_3NH_3PbI_3$ perovskite thin films based on their ultrafast (seconds), reversible chemical reaction with CH_3NH_2 gas at room temperature. The key to this healing behavior is the formation and spreading of an intermediate $CH_3NH_3PbI_3 \cdot xCH_3NH_2$ liquid phase during this unusual perovskite–gas interaction. We demonstrate the versatility and scalability of the MIDH process, and show dramatic enhancement in the performance of perovskite solar cells (PSCs) with MIDH. This study represents a new direction in the formation of defect-free films of hybrid perovskites.

The field of photovoltaics is undergoing a revolution with the introduction of solution-processed $CH_3NH_3PbI_3$ (MAPbI$_3$) perovskite thin films as light absorbers.[1–4] The ability to form high-quality perovskite thin films over large areas is critical to the research and development in this area. Thus, tremendous effort is being directed towards gaining better control over the crystallization of the perovskite from solutions,[5] which has resulted in the development of a variety of new methods.[6,7] However, solution-processes tend to be less robust, and they require exacting processing conditions. Thus, solution-processed perovskite films invariably contain defects, such as voids and pinholes. In this context, post-processing morphology-reconstruction of defective films is a more attractive approach for the formation of high-quality, large-scale perovskite films, yet there is a dearth of effort in this area. In this study, we report the discovery of room-temperature,

ultrafast methylamine-induced defect-healing (MIDH) of defective MAPbI$_3$ perovskite films. Central to this unprecedented healing behavior is the unusual chemical interaction between MAPbI$_3$ perovskite and methylamine (CH_3NH_2) gas (Figure 1).
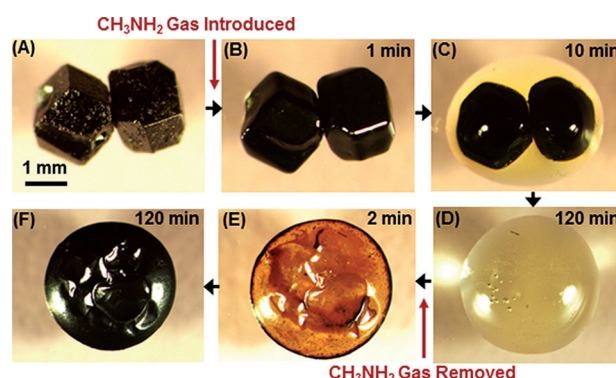

Figure 1. In situ optical microscopy of the morphology evolution of two touching MAPbI$_3$ perovskite crystals (same magnification) upon exposure to CH_3NH_2 gas and CH_3NH_2 degassing: A) before CH_3NH_2 gas exposure, B) CH_3NH_2 gas introduced, C) partial collapse of perovskite structure and conversion to liquid, D) full conversion to liquid, E) CH_3NH_2 degassing, and F) perovskite back-conversion completed.

Figure 1A shows two large, faceted MAPbI$_3$ perovskite particles (ca. 2 mm) in contact with each other. In Figure 1B, CH_3NH_2 gas is introduced, resulting in the smoothening of the crystal edges within 1 min. After 10 min, a pool of clear liquid is observed (Figure 1C), and the surface of MAPbI$_3$ perovskite crystals appear to "melt". In 120 min, the full collapse of MAPbI$_3$ perovskite crystals into the liquid is complete (Figure 1D). The liquid state of the "melted" crystals is confirmed by naked eye, as shown in Figure S1. At this point, the CH_3NH_2 gas is removed, and within 2 min, the MAPbI$_3$ perovskite begins to recrystallize, along with the darkening of the liquid (Figure 1E). After 120 min, the crystallization of MAPbI$_3$ perovskite is complete (Figure 1F) and the final fused MAPbI$_3$ perovskite particle has contracted compared with the liquid (Figure 1D). This solid–liquid conversion process is reversible, where the MAPbI$_3$ perovskite converts into a clear liquid again when CH_3NH_2 gas is reintroduced, and converts back to MAPbI$_3$ perovskite upon CH_3NH_2 degassing.

This conversion of solid MAPbI$_3$ perovskite into liquid is clearly the result of uptake of CH_3NH_2 molecules. It has been reported that the basic N atom with an electron lone pair in

[*] Dr. Z. Zhou,[+] Z. Wang,[+] Dr. S. Pang, D. Wang, Dr. H. Xu, Dr. Z. Liu, Dr. G. Cui
Qingdao Institute of Bioenergy and Bioprocess Technology
Chinese Academy of Sciences
Qingdao 266101 (P.R. China)
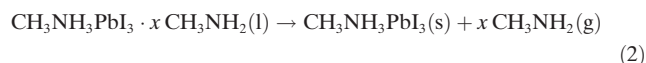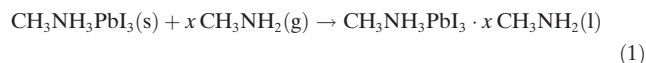E-mail: pangsp@qibebt.ac.cn
       cuigl@qibebt.ac.cn
Y. Zhou,[+] Prof. N. P. Padture
School of Engineering, Brown University
Providence, RI 02912 (USA)

[+] These authors contributed equally to this work.

alkylamine molecules interacts with the PbI_6-octahedra in the layered PbI_2 structure.[8] It is highly likely that CH_3NH_2 reacts in a similar way with the inorganic PbI_6-octahedra framework in $MAPbI_3$ perovskite, resulting in the complete collapse [Eq. (1)] of that structure into a liquid. Upon reduction of CH_3NH_2 gas partial pressure, CH_3NH_2 molecules are released from the liquid [Eq. (2)], resulting in the reconstruction of the $MAPbI_3$ perovskite structure. The commonality of the methyl group in $MAPbI_3$ and CH_3NH_2 gas appears to be responsible for the complete conversion and reversibility.

$$CH_3NH_3PbI_3(s) + x\,CH_3NH_2(g) \rightarrow CH_3NH_3PbI_3 \cdot x\,CH_3NH_2(l) \tag{1}$$

$$CH_3NH_3PbI_3 \cdot x\,CH_3NH_2(l) \rightarrow CH_3NH_3PbI_3(s) + x\,CH_3NH_2(g) \tag{2}$$

To gain further insight into this gas–perovskite interaction behavior, the effect of the type of amine gas is studied, and the results are shown in Figure S2 in the Supporting Information. When ammonia (NH_3) gas, instead of CH_3NH_2, is introduced, the intercalation of NH_3 into the crystalline structure of the $MAPbI_3$ perovskite results in photo-bleaching (Figure S2 A), similar to what has been reported earlier in the context of thin films.[9] However, the NH_3–perovskite interaction does not result in the complete collapse of the solid into a liquid. This lack of collapse is most likely due to the lower basicity and the smaller size of NH_3 compared with CH_3NH_2. Thus, only minor morphology changes occur in the perovskite after the reversible interaction with NH_3 (Figure S2 A). When larger-molecule amine gases, ethylamine ($C_2H_5NH_2$) or *n*-butyl-amine ($CH_3(CH_2)_3NH_2$), are introduced, the $MAPbI_3$ per-ovskite particles appear to "melt" as well, resulting in the formation of liquid phase of $MAPbI_3 \cdot x\,C_2H_5NH_2$ or $MAPbI_3 \cdot x\,CH_3(CH_2)_3NH_2$, respectively, accompanied by sub-stantial volume expansion and surface smoothening (Figure S2 B and Figure S2 C). However, complete back-conversion into the black $MAPbI_3$ perovskite phase does not occur after the gas is removed. Thus, for alkyl group R other than CH_3, the reaction of $CH_3NH_3I + R\text{-}NH_2 \rightarrow R\text{-}NH_3I + CH_3NH_2$ is likely to occur, resulting in the irreversible formation of a stable non-$MAPbI_3$ phase. These results highlight the importance of the rational selection of CH_3NH_2 gas for the MIDH of $MAPbI_3$ perovskite thin films.

Figure 2 A shows how the phenomenon described above is applied to perform MIDH treatment of a porous, rough $MAPbI_3$ perovskite film, converting it into a fully dense, smooth film. In MIDH experiments, visually, the raw $MAPbI_3$ perovskite film appears translucent with a dull surface. At the instant of exposure to CH_3NH_2 gas, the film appears bleached, with the formation of the intermediate liquid-phase $MAPbI_3 \cdot x\,CH_3NH_2$. Upon removal from the CH_3NH_2-gas atmos-phere, the film turns dark within 2–5 s, with a highly reflective (shiny) surface. The overall process occurs in an astonishingly short period of time, and results in the healing of the $MAPbI_3$ perovskite film from a defective state to a "perfect" state. (See Supporting Information for experimental details.) The transformation of the surface morphology of the $MAPbI_3$ perovskite film is clearly seen in the scanning electron microscope (SEM) and the atomic force microscope (AFM)
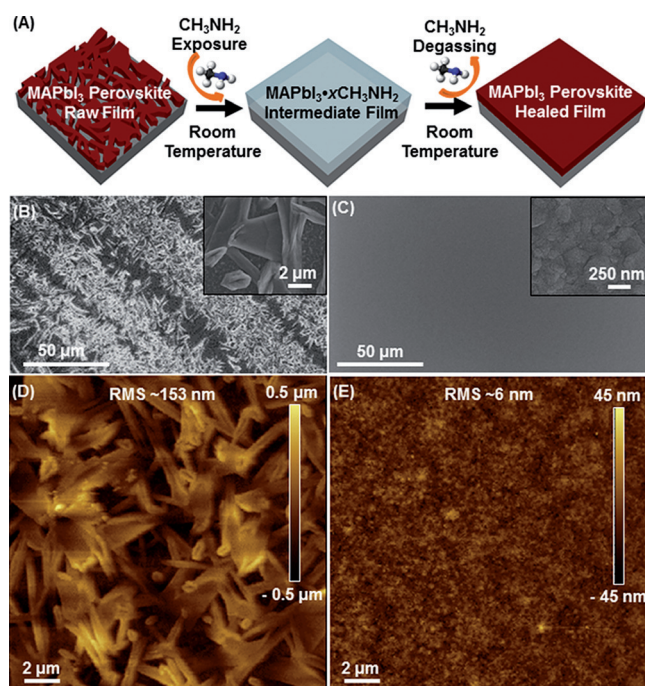

Figure 2. A) Schematic illustration of methylamine-induced defect-heal-ing (MIDH) of $MAPbI_3$ perovskite thin films. SEM micrographs of top surfaces of $MAPbI_3$ thin films: B) raw film and C) healed film; (insets: higher magnification SEM images). AFM images of top surfaces of $MAPbI_3$ perovskite thin films: D) raw film and E) healed film.

images. Figure 2 B is a SEM image of the raw $MAPbI_3$ perovskite film (ca. 250 nm thickness) prepared using the conventional one-step method. The growth of dendrite-like $MAPbI_3$ perovskite crystals, and voids between them is typical of one-step-processed perovskite films using dime-thylformamide (DMF) solvent.[10] The size of the voids in the starting raw film can reach up to several micrometers. After MIDH treatment, all the dendrite-like crystals and the voids have disappeared, and a dense, smooth $MAPbI_3$ perovskite film has emerged in its place (Figures 2 C), which is respon-sible for the visual evolution of the film from dull to shiny. Figure 2 D is an AFM topographical image of the raw $MAPbI_3$ perovskite film showing root mean square (RMS) roughness of approximately 153 nm over an $18 \times 18\ \mu m^2$ area. In contrast, the AFM topographical image of the healed film in Figure 2 E shows a remarkably dense and smooth film, with a RMS roughness of only around 6 nm.

Figure 3 A shows X-ray diffraction (XRD) patterns of the raw MAPbI3 perovskite film, $MAPbI_3 \cdot x\,CH_3NH_2$ intermedi-ate film and healed $MAPbI_3$ perovskite film on compact TiO_2-coated FTO glass substrates. The XRD pattern from the raw film confirms the typical $MAPbI_3$ perovskite phase. The XRD pattern of the $MAPbI_3 \cdot x\,CH_3NH_2$ intermediate film under CH_3NH_2 gas shows only substrate peaks, indicative of its non-crystalline nature. After CH_3NH_2 degassing, a phase-pure, 110-textured perovskite film evolves. Figure 3 B shows the XRD intensity from the rough and the healed $MAPbI_3$ perovskite films for the 110 reflection under identical measurement conditions, showing a 15-fold increase in the counts after healing. This change is indicative of higher degree
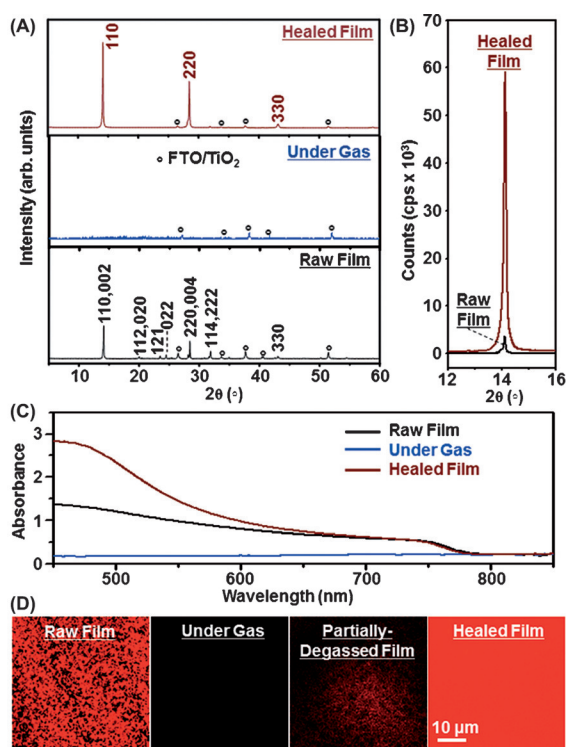
Figure 3. A) Indexed XRD patterns of the films: raw MAPbI$_3$ perovskite film, MAPbI$_3$·xCH$_3$NH$_2$ intermediate film, and healed MAPbI$_3$ perovskite film. B) XRD patterns showing the intensity counts for the 110 reflection from raw and healed MAPbI$_3$ perovskite films. C) UV/Vis absorption spectra of raw MAPbI$_3$ perovskite film, MAPbI$_3$·xCH$_3$NH$_2$ intermediate film, and healed MAPbI$_3$ perovskite film. D) In situ photoluminescence maps of a MAPbI$_3$ perovskite film during the MIDH process (same magnification): raw film, MAPbI$_3$·xCH$_3$NH$_2$ intermediate film, partially degassed film (1 s after removal of gas), and healed film (4 s after removal of gas).

of crystallinity and texture in the healed film, which is highly desirable for PSCs application.[11] Figure 3 C shows ultraviolet-visible (UV/Vis) optical absorption spectra. The raw film shows typical absorption of MAPbI$_3$ perovskite with an absorption edge at approximately 780 nm. The MAPbI$_3$·xCH$_3$NH$_2$ intermediate film shows almost no absorption, indicative of the collapse of the perovskite structure. The healed MAPbI$_3$ perovskite film recovers the absorption feature of the perovskite, but with significantly increased absorbance, especially in the 400–600 nm region. This is primarily due to the dense and uniform nature of the healed film, which prevents leakage of light through voids. Figure 3 D is a sequence of photoluminescence (PL) maps taken in situ during the MIDH process to complement the ex situ SEM, AFM, XRD, and UV/Vis studies. The non-uniform PL is consistent with the poor coverage in the raw MAPbI$_3$ perovskite film. The PL is completely quenched in the film immediately after the CH$_3$NH$_2$ gas is introduced, further confirming the absence of luminescing crystalline perovskite. Upon CH$_3$NH$_2$ degassing, the weak PL signal gradually recovers from localized areas, which indicates the nucleation of MAPbI$_3$ perovskite. Finally, uniform, stronger PL signal is observed over the entire area in the healed MAPbI$_3$ perovskite film.

We also demonstrate that the MIDH process is independent of the morphology of the starting films, where raw MAPbI$_3$ perovskite films with different types of common "defective" morphologies, deposited using a variety of solution-processing methods, can be healed to nearly the same "perfect" state using MIDH (Figures S3–S5). In particular, we show that commercial large-area (several cm^2) MAPbI$_3$ perovskite films deposited using the slot-die coating process can be fully healed using the MIDH process (Figure S6).

Based on all the results presented herein, the basic mechanisms involved in the MIDH of MAPbI$_3$ perovskite thin films are depicted schematically in Figure 4. Exposure to
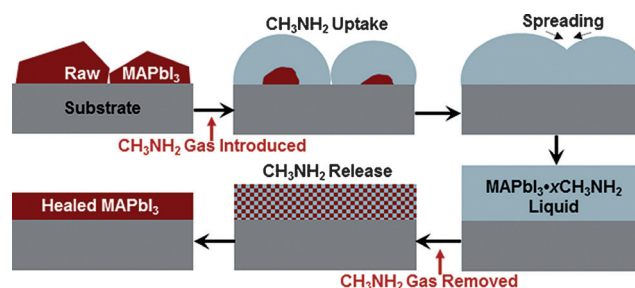

Figure 4. Schematic illustration of the mechanisms involved in the MIDH of MAPbI$_3$ perovskite films.

CH$_3$NH$_2$ gas results in the uptake of CH$_3$NH$_2$ molecules by the raw MAPbI$_3$ perovskite film accompanied by a volume expansion, collapse of the perovskite structure, and the formation of a clear liquid. This occurs in a very short time because of the nanoscale of the MAPbI$_3$ crystals in the thin films. The liquid spreads instantaneously owing to wetting of the substrate, and forms an ultra-smooth surface. In the case of mesoscopic-oxide layer on the substrate, the liquid is likely to infiltrate readily into the mesoporous structure. Upon removal of the CH$_3$NH$_2$-gas atmosphere, the liquid releases CH$_3$NH$_2$ molecules rapidly, once again, a result of the nanoscale of the liquid MAPbI$_3$·xCH$_3$NH$_2$ film. This release results in volume contraction, and rebuilding of the perovskite structure by rapid nucleation and growth, ultimately resulting in an ultra-smooth and dense MAPbI$_3$ thin film. Thus, the liquid state of the intermediate phase is critical to the healing process. This is further supported by the fact that the morphological defects of the raw MAPbI$_3$ films can also be healed using C$_2$H$_5$NH$_2$ or CH$_3$(CH$_2$)$_3$NH$_2$) gases (Figure S7C–S7D), where a liquid intermediate phase forms (Figures S2B–S2C), but not NH$_3$ gas (Figure S7B), where the liquid intermediate phase is absent (Figure S2A). However, in the C$_2$H$_5$NH$_2$ or CH$_3$(CH$_2$)$_3$NH$_2$ cases, the pure MAPbI$_3$ perovskite phase is not recovered, which is consistent with the in situ optical microscopy observations.

The effect of MIDH treatment on the performance of MAPbI$_3$-based PSCs is shown in Figure 5. Figure 5 A and 5 B are cross-sectional SEM images of the PSCs with raw and healed MAPbI$_3$ perovskite films, respectively. In the case of the healed film, the mesoporous TiO$_2$ layer is fully infiltrated with MAPbI$_3$ perovskite, and the dense MAPbI$_3$ perovskite
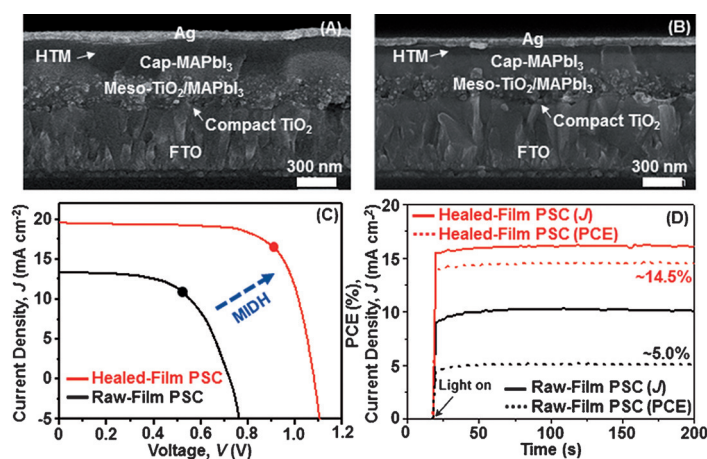
Figure 5. Cross-sectional SEM images of mesoscopic PSCs using: A) raw MAPbI$_3$ perovskite film and B) healed MAPbI$_3$ perovskite film. (C) J–V characteristics of the mesoscopic PSCs using raw and healed MAPbI$_3$ perovskite films (reverse scan; maximum power points denoted by solid circles). (D) Stabilizing PCE and J output at maximum power points of the PSCs.

"capping" layer shows smooth, uniform coverage (Figure 5 B and Figure S8). The current-density (J)–voltage (V) responses in Figure 5 C show obvious increase in all performance parameters (short circuit current J_{SC}: from 13.5 mA cm^{-2} to 19.6 mA cm^{-2}; open circuit voltage V_{OC}: from 0.72 V to 1.08 V; fill factor FF: from 0.586 to 0.714) with MIDH treatment. A significant increase in the overall power conversion efficiency (PCE), from 5.7 % to 15.1 %, is observed, which is clearly the result of the improved film morphology. The J_{SC} values are consistent with the external quantum efficiency (EQE) measurements presented in Figure S9. Since typical hysteresis (Figure S10) still exists in both PSCs, the maximum-power-point J, which is then converted into PCE, is monitored as shown in Figure 5 D. The stabilizing PCE output at the maximum power point increases from 5.0 % to 14.5 %, further confirming the efficiency enhancement in PSCs with MIDH treatment. (PCEs statistics are presented in Figure S11.)

In summary, the room-temperature MIDH approach introduced herein provides an unprecedented capability for the processing of high-quality, uniform MAPbI$_3$ perovskite films over large-areas for high-performance PSCs and beyond. The ultrafast and facile nature of the MIDH process is compatible with established scalable thin-film processing technologies, as demonstrated in Figure S6. Furthermore, the concept of morphology-engineering based on reversible gas–solid interaction could be extended to a board range of organo-metal halide compounds. This approach opens a new direction in the formation of defect-free, large-area organo-metal halide materials.

Experimental Section

MIDH Procedure: The starting raw MAPbI$_3$ perovskite films were deposited using the conventional one-step method. A 40 wt% PbI$_2$:MAI (molar ratio 1:1) solution in *N*,*N*-dimethylformamide (DMF) was spin-coated (4000 rpm, 45 s) on compact TiO$_2$-coated FTO glass, followed by a heat-treatment at 100 °C for 10 min. Subsequently, the raw MAPbI$_3$ perovskite films were simply placed in the CH$_3$NH$_2$ gas environment for 2–3 s at room temperature, and were then removed to the ambient quickly.

Materials Characterization: XRD patterns were obtained using an X-ray diffractormeter (D8 Advance, Bruker, Germany) using Cu Kα radiation, with 0.02° step and 2 s/step dwell. UV/Vis absorption spectra of the perovskite films were recorded using spectrometer (U-4100, Hitachi, Japan). UV/Vis measurements on the films under CH$_3$NH$_2$ gas were performed on samples sealed in quartz. A field-emission SEM (S-4800, Hitachi, Japan) was used to observe the top surfaces and cross-sections. AFM measurements were performed in contact mode using AFM microscope (5400, Agilent, USA). In situ PL mapping was conducted using a confocal laser scanning microscope (Fluo ViewTM FV1000, Olympus, Japan). The in situ optical microscopy observation of two MAPbI$_3$ perovskite particles was carried out using a stereomicroscope (SZX16, Olympus, Japan).

Solar Cell Fabrication and Performance Measurement: The MAPbI$_3$ perovskite layer was then deposited on 250 nm thick mesoporous TiO$_2$ (on compact TiO$_2$-coated FTO glass) with or without the MIDH treatment as described above. The hole transporting material (HTM) was then deposited by spin-coating (3000 rpm, 30 s), followed by evaporation of 50 nm Ag layer to complete the solar cells. J–V characteristics of the as-fabricated PSCs were measured using a 2400 Sourcemeter (Keithley, USA) under simulated one-sun AM 1.5G 100 mW cm^{-2} intensity (Oriel Sol3A Class AAA, Newport, USA), under both reverse (from V_{OC} to J_{SC}) and forward (from J_{SC} to V_{OC}) scans. The maximum-power output stability of the PSCs was measured by monitoring the J output at the maximum-power V bias (deduced from the reverse-scan J–V curves). Typical active area of the PSCs is 0.09 cm^2 defined using non-reflective metal mask. External quantum efficiency (EQE) measurements were carried out on an EQE measurement setup (Newport, USA).

More detailed description of the experimental procedures, and additional results, are included in the supporting information.

[1] a) A. Kojima, K. Teshima, Y. Shirai, T. Miyasaka, *J. Am. Chem. Soc.* **2009**, *131*, 6050–6051; b) J.-H. Im, C.-R. Lee, J.-W. Lee, S.-W. Park, N.-G. Park, *Nanoscale* **2011**, *3*, 4088–4093; c) H.-S. Kim, C.-R. Lee, J.-H. Im, K.-B. Lee, T. Moehl, A. Marchioro, S.-J. Moon, R. Humphrey-Baker, J.-H. Yum, J. E. Moser, M. Grätzel, N.-G. Park, *Sci. Rep.* **2012**, *2*, 591.

[2] a) M. M. Lee, J. Teuscher, T. Miyasaka, T. N. Murakami, H. J. Snaith, *Science* **2012**, *338*, 643–647; b) J. Burschka, N. Pellet, S.-J. Moon, R. Humphrey-Baker, P. Gao, M. K. Nazeeruddin, M. Grätzel, *Nature* **2013**, *499*, 316–319.

[3] a) H. J. Snaith, *J. Phys. Chem. Lett.* **2013**, *4*, 3623; b) M. Grätzel, *Nat. Mater.* **2014**, *13*, 838–842.

[4] a) M. A. Green, A. Ho-Baillie, H. J. Snaith, *Nat. Photonics* **2014**, *8*, 506; b) H. S. Jung, N.-G. Park, *Small* **2015**, *11*, 10–25.

[5] Y. Zhao, K. Zhu, *J. Phys. Chem. Lett.* **2014**, *5*, 4175–4186.

[6] a) M. Xiao, F. Huang, W. Huang, Y. Dkhissi, Y. Zhu, J. Etheridge, A. Gray-Weale, U. Bach, Y.-B. Cheng, L. Spiccia, *Angew. Chem. Int. Ed.* **2014**, *53*, 9898–9903; *Angew. Chem.* **2014**, *126*, 10056–10061; b) Y. Kutes, L. Ye, Y. Zhou, S. Pang, B. D. Huey, N. P. Padture, *J. Phys. Chem. Lett.* **2014**, *5*, 3335–3339; c) Y. Zhou, M. Yang, W. Wu, A. L. Vasiliev, K. Zhu, N. P. Padture, *J. Mater. Chem. A* **2015**, *3*, 8178–8184; d) Y. Zhou, M.

Yang, A. L. Vasiliev, H. F. Garces, Y. Zhao, D. Wang, S. Pang, K. Zhu, N. P. Padture, *J. Mater. Chem. A* **2015**, *3*, 9249–9256.

[7] a) N. J. Jeon, J. H. Noh, Y. C. Kim, W. S. Yang, S. Ryu, S. I. Seok, *Nat. Mater.* **2014**, *13*, 897–903; b) Z. Xiao, C. Bi, Y. Shao, Q. Dong, Y. Yuan, C. Wang, Y. Gao, J. Huang, *Energy Environ. Sci.* **2014**, *7*, 2619–2623; c) Q. Chen, H. Zhou, Z. Hong, S. Luo, H.-S. Duan, H.-H. Wang, Y.-S. Liu, G. Li, Y. Yang, *J. Am. Chem. Soc.* **2014**, *136*, 622–625.

[8] R. F. Warren, W. Y. Liang, *J. Phys. Condens. Matter* **1993**, *5*, 6407.

[9] Y. Zhao, K. Zhu, *Chem. Commun.* **2014**, *50*, 1605–1607.

[10] D. Wang, Z. Liu, Z. Zhou, H. Zhu, Y. Zhou, C. Huang, Z. Wang, H. Xu, Y. Jin, B. Fan, S. Pang, G. Cui, *Chem. Mater.* **2014**, *26*, 7145–7150.

[11] E. Edri, S. Kirmayer, A. Henning, S. Mukhopadhyay, K. Gartsman, Y. Roesenwaks, G. Hodes, D. Cahen, *Nano Lett.* **2014**, *14*, 1000–1004.